

# Greenland Ice Sheet runoff reduced by meltwater refreezing in bare ice

**Matthew Cooper** (✉ [guycooper@ucla.edu](mailto:guycooper@ucla.edu))

Pacific Northwest National Laboratory <https://orcid.org/0000-0002-0165-209X>

**Laurence Smith**

Brown University

**Åsa Rennermalm**

Department of Geography, Rutgers, The State University of New Jersey

**Kang Yang**

University of California, Los Angeles (UCLA) <https://orcid.org/0000-0002-7246-8425>

**Glen Liston**

Colorado State University

**Jonathan Ryan**

Brown University <https://orcid.org/0000-0002-9432-1512>

**Dirk van As**

Geological Survey of Denmark and Greenland

**Lincoln Pitcher**

University of Colorado, Boulder <https://orcid.org/0000-0001-8624-9760>

**Clément Miège**

University of Utah

**Sarah Cooley**

Department of Geography, University of Oregon

**Brandon Overstreet**

Department of Geology and Geophysics, University of Wyoming

---

## Physical Sciences - Article

**Keywords:** Greenland Ice Sheet, global sea-level rise, meltwater, ice sheet runoff

**Posted Date:** August 26th, 2021

**DOI:** <https://doi.org/10.21203/rs.3.rs-842710/v1>

**License:** © ⓘ This work is licensed under a Creative Commons Attribution 4.0 International License.

[Read Full License](#)

---



## **Greenland Ice Sheet runoff reduced by meltwater refreezing in bare ice**

Matthew G. Cooper<sup>1,2,\*</sup>, Laurence C. Smith<sup>3,4</sup>, Åsa K. Rennermalm<sup>5</sup>, Kang Yang<sup>6,7,8</sup>, Glen E. Liston<sup>9</sup>, Jonathan C. Ryan<sup>10</sup>, Dirk van As<sup>11</sup>, Lincoln H Pitcher<sup>12</sup>, Clément Miège<sup>5,13</sup>, Sarah W. Cooley<sup>10</sup>, Brandon T. Overstreet<sup>14</sup>

<sup>1</sup>Department of Geography, University of California, Los Angeles, Los Angeles, CA 90095, USA

<sup>2</sup>Atmospheric Science & Global Change Division, Pacific Northwest National Laboratory, Richland, WA 99354, USA

<sup>3</sup>Institute at Brown for Environment and Society, Brown University, Providence, RI 02912, USA

<sup>4</sup>Department of Earth, Environmental and Planetary Sciences, Brown University, Providence, RI 02912, USA

<sup>5</sup>Department of Geography, Rutgers, The State University of New Jersey, Piscataway, NJ 08854, USA

<sup>6</sup>School of Geography and Ocean Science, Nanjing University, Nanjing, China

<sup>7</sup>Jiangsu Provincial Key Laboratory of Geographic Information Science and Technology, Nanjing, China

<sup>8</sup>Southern Marine Science and Engineering Guangdong Laboratory, Zhuhai, China

<sup>9</sup>Cooperative Institute for Research in the Atmosphere, Colorado State University, Fort Collins, CO 80523, USA

<sup>10</sup>Department of Geography, University of Oregon, Eugene, OR 97403, USA

<sup>11</sup>Geological Survey of Denmark and Greenland, Copenhagen, Denmark

<sup>12</sup>Cooperative Institute for Research in Environmental Sciences, University of Colorado, Boulder, CO 80309, USA

<sup>13</sup>Department of Geography, University of Utah, Salt Lake City, UT 84112, USA

<sup>14</sup>Department of Geology and Geophysics, University of Wyoming, Laramie WY 82070, USA

**The Greenland Ice Sheet's contribution to global sea-level rise is accelerating<sup>1</sup> due to increased melting of its bare-ice ablation zone<sup>2-6</sup>, but there is growing evidence that climate models overestimate runoff from this critical area of the ice sheet<sup>7-12</sup>. Current climate models assume all bare-ice runoff escapes to the ocean, unlike snow-covered areas where some fraction of runoff is retained and/or refrozen in porous firn<sup>13-15</sup>. Here we use in situ measurements and numerical modeling to reveal extensive retention and refreezing of liquid meltwater in bare glacial ice, explaining chronic runoff overestimation by climate models. From 2009–2018, refreezing of liquid meltwater in bare, porous glacial ice reduced meltwater runoff by 11–23 Gt a<sup>-1</sup> in southwest Greenland alone, equivalent to 10–20% of annual meltwater production. This mass retention is commensurate with current estimates of climate model ice sheet meltwater runoff uncertainty, and may represent an overlooked buffer on projected runoff increases for the coming century<sup>16</sup>. Inclusion of bare-ice retention and refreezing processes in climate models therefore has immediate potential to improve forecasts of ice sheet runoff and its contribution to global sea-level rise.**

## Main

Greenland Ice Sheet (GrIS) mass loss raised global sea level  $10.8 \pm 0.9$  mm between 1992–2018 and climate models forecast an additional 70–130 mm by year 2100<sup>1</sup>. Most of this recent mass loss can be attributed to increased meltwater runoff from the ablation zone<sup>2–6</sup>. Within this critically important zone, winter snowpack melts entirely each summer exposing dark, bare glacier ice that absorbs up to three times as much sunlight as bright snow<sup>17</sup>. Increasing temperatures and reduced summer snowfall have exposed larger areas of bare ice in recent decades<sup>2,3,18</sup>, driving enhanced surface melting in the ablation zone<sup>2–4</sup>. Understanding the fate of meltwater from Greenland’s growing bare-ice zone is therefore critical for accurate modeling of sea levels<sup>16</sup>.

Climate models track energy and mass budgets on the ice sheet surface and are the primary tools available to predict future ice sheet runoff<sup>13,19</sup>. However, there is extensive evidence that climate models overestimate runoff from bare ice surfaces<sup>7–12</sup>. In Greenland’s melt-intensive southwest sector, river discharges measured at the ice sheet periphery reveal up to 67% less annual meltwater release to surrounding oceans than climate model calculations<sup>7,9–11</sup>. Supraglacial lakes that form on the ice sheet surface fill at slower rates than predicted by climate models<sup>12</sup>, and direct measurements of supraglacial runoff are overpredicted by +21–58% during peak summer melt conditions<sup>8</sup>. Climate models overestimate surface melt by +14–40% relative to satellite laser altimetry measurements<sup>20</sup>, by -17% (at one ablation-zone site) to +10–43% (at four other ablation-zone sites) relative to point ablation stake measurements<sup>21,22</sup>, and overestimate ice sheet mass changes by +21–47% relative to GRACE satellite gravity retrievals<sup>23,24</sup>. These discrepancies are not explained by errors in modeled surface energy balance components, which closely correlate with in situ meteorological observations<sup>8,21,22</sup>.

An explanation for why climate models currently overestimate ice sheet runoff may be their conceptual treatment of bare ice surfaces as an impervious, high-density substrate with no capacity to retain water<sup>13–15</sup>. Accordingly, runoff produced on bare ice is instantly credited in its entirety to sea level<sup>14</sup>, despite growing field reports of non-trivial meltwater retention on or within bare ice<sup>7,8,25–29</sup>. These studies suggest that bare ice surfaces are not necessarily impervious, but can behave rather like snow and firn, with some portion of generated meltwater retained either through refreezing or liquid storage in pore spaces<sup>30,31</sup>. Because bare ice comprises >80% of the ablation zone by surface area and generates >85% of meltwater runoff<sup>2</sup>, even small amounts of meltwater retention or refreezing would constitute a substantial overlooked component of the ice sheet surface mass balance and explain consistent reports of climate model runoff overestimation from bare ice surfaces<sup>7,8,12</sup>.

Reconciling climate model calculations with real-world runoff measurements is difficult because direct measurements of runoff on the ice sheet surface, prior to interference from englacial and subglacial processes, are extremely rare<sup>7,11</sup>. Here, we pair numerical surface mass balance modeling with in situ measurements of meltwater runoff<sup>8</sup> and bare ice properties<sup>26,32</sup> from a well-studied surface catchment on the southwest GrIS bare-ice ablation zone. We then reconcile discrepancies between modeled and observed meltwater runoff by quantifying retention and refreezing processes in bare ice over the entire southwest GrIS ablation zone, where the majority of GrIS surface mass loss originates<sup>2,3</sup>.

### **Climate models overestimate meltwater runoff on the bare-ice ablation zone**

Rio Behar is a supraglacial river on the southwest GrIS ablation zone that drains an ~60–63 km<sup>2</sup> catchment, depending on year<sup>8,12,33</sup> (Figure S1). Our previous field measurements during July 2015 found that regional and global climate models overpredicted Rio Behar runoff by +21–

58%<sup>8</sup>. During a 6–13 July 2016 field experiment we revisited the site to collect a seven-day record of 168 consecutive hourly discharges<sup>34</sup>, concurrent with three-hourly ice surface lowering measurements from a network of ablation stakes installed near the gauging site (Methods and Figure S2). Shallow ice cores collected at the same site in July 2016 revealed that the bare-ice surface was porous and saturated with meltwater, with an average bare-ice density of just 690 kg m<sup>-3</sup> within the upper 1.1 m of ice<sup>26</sup>. Here, these measured discharges (hereafter ‘runoff’), surface lowering rates, and physical ice properties are compared with simulated meltwater production and runoff from two regional climate models, a global climate reanalysis model, and a numerical model of spectral radiation and thermodynamic heat transfer developed for bare glacial ice<sup>35</sup> (Methods).

Consistent with previous studies<sup>7–12</sup>, we find that climate model values of runoff overpredict measured meltwater runoff (Figure 1). By the end of the 6–13 July 2016 field experiment, climate model runoff ranges from -13% lower (MERRA-2) to +53% higher (RACMO2.3) than observations, with all but MERRA-2 exceeding observed runoff values (Figure 1). Among the climate models examined here, RACMO2.3 most closely reproduces observed albedo and net radiative heat fluxes, yet severely overpredicts runoff despite good representation of these critical surface energy balance components (Figure S4 and Figure S5).

To explain these discrepancies between observations and climate models, we developed a process-based numerical model of ice sheet meltwater runoff that we call ‘SkinModel’ (Methods). SkinModel represents the ice sheet surface as an infinitely thin, hydrologically impermeable ‘skin’ layer of high-density (900 kg m<sup>-3</sup>) ice with zero heat capacity, emulating the assumption used in climate models for bare glacial ice (Methods Equation 1)<sup>14</sup>. SkinModel is forced on an hourly timestep with meteorological observations recorded by the PROMICE/GAP

KAN\_M surface-based automatic weather station<sup>36</sup> located ~2 km from the Rio Behar catchment. To first establish whether SkinModel effectively emulates climate model meltwater runoff predictions, we force SkinModel with surface albedo values output from each climate model (rather than KAN\_M albedo values), and find its predictions are virtually identical to climate model predictions (Figure 1; dashed vs solid lines). Note that all model forcings besides albedo are kept consistent across these emulator simulations, signifying that differences in ice surface albedo alone drive virtually all differences between climate model predictions of runoff shown in Figure 1.

Next, we force SkinModel with values of albedo recorded at KAN\_M, and find that modeled runoff is +43% higher than measured runoff (Figure 1; green solid line). Weather station forcings thus yield runoff predictions much like RACMO2.3, the model with the most accurate albedo for this time and location. Similar results are found when the same models are tested using the same methods against our earlier field measurements from 2015<sup>8</sup> (Figure S6). Even larger runoff overestimation is simulated if calibrated MODIS satellite albedo values<sup>37</sup> (Figure S7) are used as model forcing. This reveals that among the climate models examined here, accurate representation of ice surface albedo leads to overpredicted runoff, whereas accurate predictions of runoff are a fortuitous result of unrealistically high albedo (Figure 1).

### **Runoff overestimation explained by meltwater refreezing in bare ice**

We developed a second process-based numerical model of ice sheet meltwater runoff that we call ‘IceModel’ (Methods). IceModel updates an earlier model of spectral radiative and thermodynamic heat transfer in glacier ice<sup>35</sup> with a field-calibrated constraint<sup>32</sup> on shortwave radiation absorption enhancement by dark impurities present within Greenland’s bare, ablating ice. In contrast to SkinModel, IceModel simulates an ice column with time-varying ice, air, water

vapor, and liquid water content (Methods Equation 3), informed by measurements of physical ice surface properties collected during a multi-year series of field campaigns on the GrIS bare-ice ablation zone<sup>7,8,11,26,32,33,38</sup>. A critical feature of IceModel is that it allows sunlight to penetrate bare ice, thus allowing melt within the ice subsurface<sup>39</sup> rather than expending all available energy upon an infinitely thin ‘skin’ surface layer.

IceModel simulations reveal that, during daylight hours, penetration of shortwave radiation produces an isothermal ice column ~1.2 m thick that stores latent heat in the form of liquid meltwater, a phenomenon independently validated by our field observations of saturated porous ice extending at least 1.1 m below the ice surface<sup>26</sup>. Lateral transport of meltwater generated within isothermal bare ice is constrained by its low horizontal hydraulic conductivity  $\mathcal{O}(10^{-2}\text{--}10^{-4} \text{ m h}^{-1})$ <sup>40,41</sup> and impermeable lower boundary<sup>3</sup>. At night, the cold atmospheric boundary layer cools the ice surface to  $-5^{\circ}\text{C}$  on average during July at this location, as indicated by IceModel simulated surface temperatures that closely track observations (Figure 2). This cold surface drives refreezing of subsurface liquid meltwater at rates approaching  $0.002 \text{ m hr}^{-1}$  between 02:00–04:00 local time, when the ice surface temperature drops as low as  $-6^{\circ}\text{C}$ . The runoff overestimation shown in Figure 1 can therefore be explained by nocturnal refreezing of liquid meltwater stored within the upper decimeters of the porous bare ice matrix. Inclusion of this process enables IceModel to reproduce observed cumulative runoff to within 3%, well within catchment boundary uncertainty (Figure 1).

Climate model mass loss overpredictions indicated in the catchment-scale runoff comparison are mirrored in rates of ice surface lowering measured at our network of ablation stakes and at the KAN\_M AWS (Figure 3a). Unlike SkinModel and the climate models it emulates, IceModel predicts internal mass loss below the ice surface caused by subsurface

absorption of transmitted solar radiation (Figure 3b). Modeled values of ice density vary from  $<300 \text{ kg m}^{-3}$  in the upper decimeter of ice to  $900 \text{ kg m}^{-3}$  below  $\sim 1.2 \text{ m}$ , with a column-averaged value of  $669 \text{ kg m}^{-3}$ , within 2% of our measured column-average ice density  $681 \text{ kg m}^{-3}$  (and well below the canonical  $900 \text{ kg m}^{-3}$  value assumed in climate model simulations, Figure 3b). Together, these model simulations and field measurements reveal that substantial meltwater generation occurs beneath the ice surface, where meltwater is retained within porous bare ice, undetected by climate model simulations of the ‘skin’ energy balance, and available for nocturnal refreezing.

### **Independent validation across the southwest Greenland Ice Sheet**

Extension of our meltwater runoff simulations to all bare-ice areas of southwest Greenland over the decade 2009–2018 (Figure 4a) validates our catchment-scale experimental conclusions. Comparison with independent measurements<sup>42</sup> of cumulative meltwater runoff discharged from a  $1250 \text{ km}^2$  catchment spanning the western Greenland ablation zone reveals an identical pattern of climate model mass loss overprediction over four consecutive years of record melting (2009–2012) (Figure 4b,c). Much like our catchment-scale simulations, when our climate model emulator SkinModel is forced with MODIS satellite retrievals of ice surface albedo<sup>37</sup>, observed ocean-going meltwater runoff is overpredicted by +51% (Figure 4c). In contrast, when IceModel is forced with observed surface albedo, runoff is +5% higher than observations, cumulative over four years, with upper and lower estimates contained entirely within  $\pm 15\%$  measurement uncertainty. This +5% overprediction of ocean-going runoff is consistent with observations of englacial and subglacial water storage in this region of the ice sheet<sup>27,28</sup>, an additional ablation-zone retention sink not represented in current climate models. Our catchment-scale conclusions are further validated by comparison with discharge measured

over seven years in the Akuliarusiarsuup Kuua River's northern tributary (AK4) (Figure S8) and with satellite estimates of supraglacial lake volume (SLV) infilling rate (a proxy for cumulative meltwater runoff<sup>12</sup>) at two sites near the Rio Behar catchment (Figure 4b). For these SLV sites, climate model runoff is +70% higher than satellite-derived runoff, whereas IceModel runoff closely tracks SLV observations (Figure 4d).

All of this suggests that the conversion of energy (input) to mass (output) is less efficient in bare ice than currently thought, thus decreasing the true export of meltwater runoff from the ice sheet surface to surrounding oceans. Once refrozen, meltwater must thaw again to become runoff, an additional energy expenditure not currently accounted for in climate models. To demonstrate the magnitude of this unrepresented energy sink, IceModel simulations indicate an annual average runoff reduction of 11 Gt a<sup>-1</sup> in Greenland's southwest sector alone due solely to refreezing of subsurface liquid meltwater in bare ice during July and August. This bare-ice refreezing estimate is equivalent to 18% of the ~63 Gt a<sup>-1</sup> annual refreezing in snow and firn predicted by MAR3.10 and RACMO2.3 for this sector of the ice sheet, or 10% of the ~116 Gt a<sup>-1</sup> annual runoff. This estimate is conservative due to our use of minimum plausible bare-ice extent (Methods) and exposure (July–August) in its calculation, but is commensurate with current lower-bound estimates of ice sheet runoff uncertainty<sup>43,44</sup>. Longer periods of below-freezing air temperatures during seasonal transitions from melt to freeze-up similarly consume melt energy, potentially increasing runoff retention on bare ice up to 23 Gt a<sup>-1</sup> (~20% of sector runoff) when considering June–September as an upper limit on seasonal bare ice exposure.

### **Implications for sea level rise predictions**

Our comparison of in situ meltwater runoff measurements collected on Greenland's ablating bare-ice surface with runoff predictions from a suite of global and regional climate

models finds that the latter overestimate runoff, here by up to +53%. The two models that do match observed runoff with reasonable accuracy (MERRA-2, MAR3.10) do so only incidentally, by overestimating albedo (i.e., by error cancellation). The underlying reason for this consistent tendency of climate models to overestimate runoff generation in the ablation zone<sup>7–12</sup> has not previously been identified, signifying a critical gap in predictive capacity concerning future ice sheet surface mass loss. Here, we show that over-prediction of runoff by climate models is explained by nocturnal refreezing of meltwater generated in the bare-ice ablation zone, a process observed on mountain glaciers<sup>45,46</sup> that has eluded detection in Greenland and is not currently included in climate model predictions of ice sheet runoff contributions to sea level rise<sup>14</sup>, nor their uncertainty<sup>43,47</sup>.

Regional climate models are the primary tools used to estimate the amount of runoff exported from Greenland's ablation zone to the global ocean (and the only tool for predicting future ice mass changes), but these models currently lack representation of the important nocturnal refreezing/retention process described here. Refreezing in snow and firn has potential to delay sea level rise by ~10–17 Gt a<sup>-1</sup> at the centennial timescale<sup>30</sup>, yet refreezing in bare ice, currently set to zero in regional climate models<sup>14</sup>, may already exceed these levels, with unknown response to continued surface warming and associated expansion of bare ice areas<sup>2</sup>. With nearly all (85–93%) of Greenland's meltwater runoff currently sourced from bare ice, these findings suggest the need to consider mechanisms of meltwater retention within Greenland's bare-ice ablation zone, in addition to snow and firn processes, to accurately inform future sea level predictions.

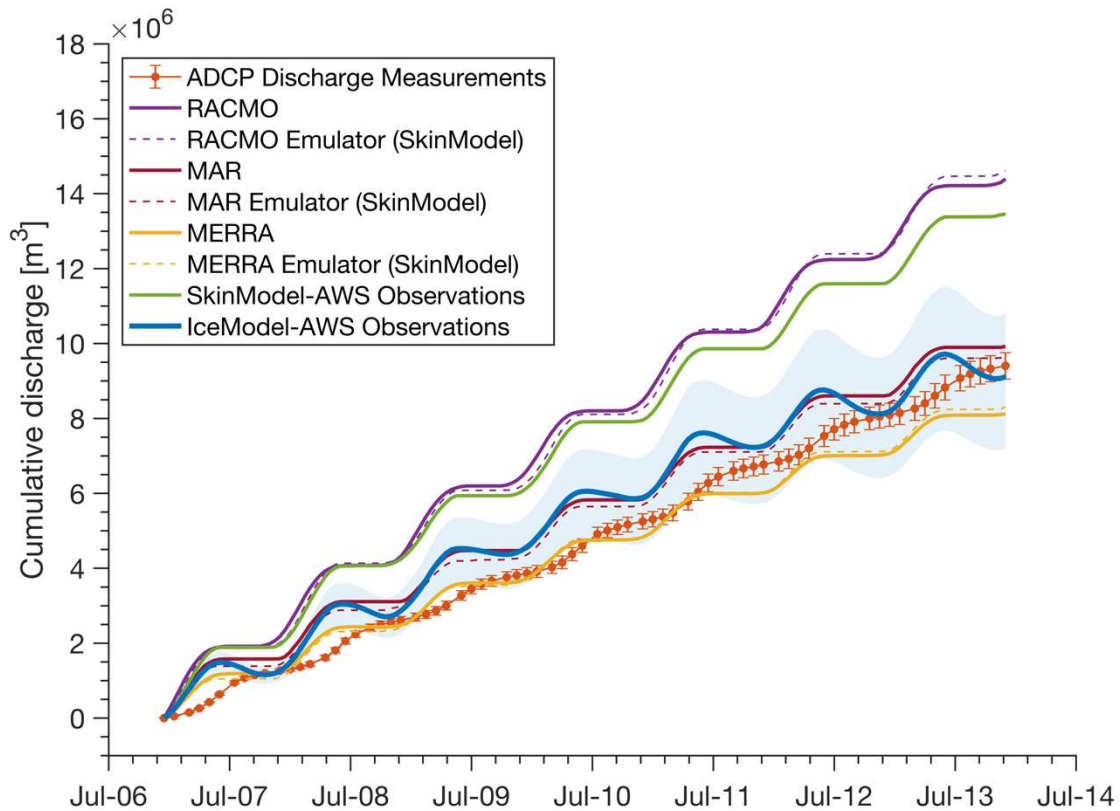


Figure 1: Climate model cumulative runoff predictions for the 6–13 July 2016 field experiment compared with direct ADCP discharge measurements, predictions from our zero-dimensional climate model surface energy balance emulator (SkinModel), and our one-dimensional mass and heat transfer model that includes subsurface meltwater production and refreezing in bare ice (IceModel). When SkinModel is deliberately forced with albedo output from each climate model, its predictions are virtually identical with those of each model (dashed lines vs solid lines). When SkinModel is forced with observed albedo recorded by automatic weather station near our experimental site, measured runoff is overpredicted (green solid line), demonstrating that accurate representation of ice-surface albedo leads to runoff overestimation at this time and location. In contrast, meltwater runoff is closely reproduced by IceModel. Solid and dashed lines represent volumetric runoff from upstream catchment area (60.04 km<sup>2</sup>). Shaded uncertainty bounds represent conservative lower (48.4 km<sup>2</sup>) and upper (71.3 km<sup>2</sup>) bounds on catchment area (Methods). Error bars on measured discharge are one standard deviation in sub-hourly discharge (Methods).

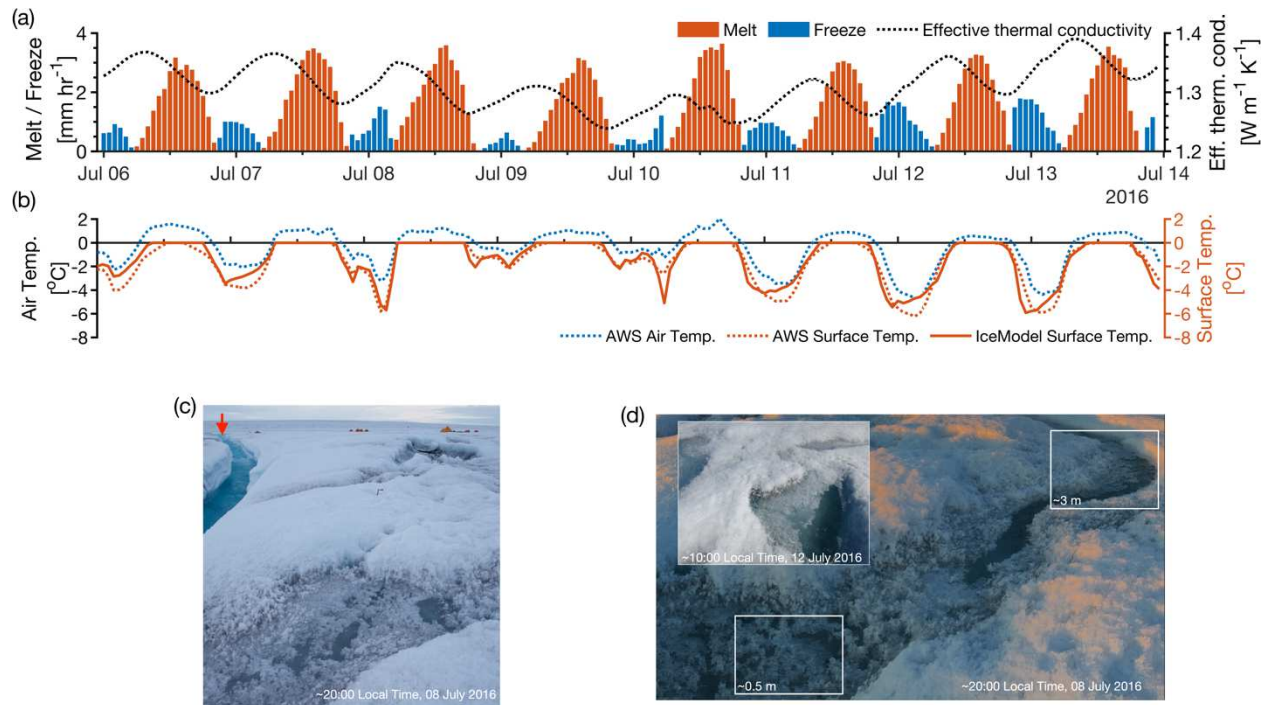


Figure 2: (a) IceModel simulations of meltwater production, refreezing, effective thermal conductivity, and (b) ice sheet surface temperature closely track diurnal variations in observed air temperature and ice sheet surface temperature during the seven-day field experiment. As liquid meltwater within the ice matrix freezes, the effective thermal conductivity (black dotted line) of the upper decimeters of ice matrix increases because ice has  $\sim 4$  times higher thermal conductivity than liquid water. The increase in thermal conductivity during nocturnal freeze enhances heat loss to the atmosphere and cold content development in the upper ice layers that inhibits runoff generation when daytime solar heating commences. Main tick marks in (a) and (b) are at 00:00 local time (UTC-2), minor tick marks are 12:00. (c-d) Photographs taken during the field experiment show refrozen meltwater entrained on the weathered bare-ice surface at night and into the early morning when low sun angles and cold air kept surface temperatures below freezing. Inset in (d) shows surficial refrozen meltwater persisting to 10:00 local time on 12 July 2016 following the coldest night during the seven-day field experiment. The approximate location of the discharge gauge station is indicated by arrow in (c) with field camp tents visible at right. Photos are by the first author.

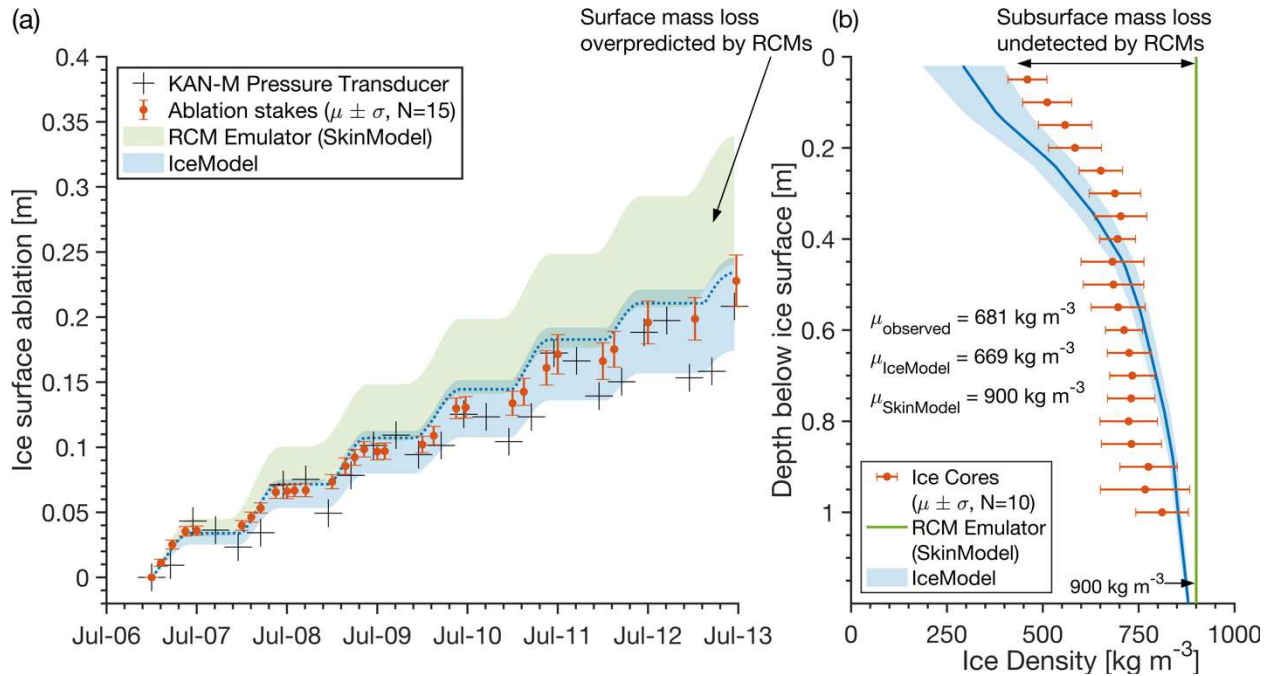


Figure 3: (a) Ice surface ablation values recorded by the KAN\_M automatic weather station (black crosses proportional to  $\pm 1$  cm instrument uncertainty) and measured values from a network of ablation stakes in the Rio Behar experimental catchment (red error bars  $\pm 1$  standard deviation). Measured ablation is closely reproduced by our one-dimensional ice column mass and heat transfer model ‘IceModel’ but is overpredicted by our climate model emulator ‘SkinModel’. The green and blue envelopes are SkinModel and IceModel meltwater production converted to ice thickness using a lower ( $600 \text{ kg m}^{-3}$ ) and upper ( $900 \text{ kg m}^{-3}$ ) assumed ice density. The dotted blue line in (a) is IceModel thickness change computed directly from the modeled vertical column ice density, shown in (b) as solid blue line with shaded envelope representing  $\pm 1$  standard deviation in modeled ice density during the field experiment. The column-averaged modeled ice density ( $\mu = 669 \text{ kg m}^{-3}$ ) is within 2% of measured ice density ( $\mu = 681 \text{ kg m}^{-3}$ ) obtained from 10 shallow ice cores collected in the Rio Behar catchment on 11–12 July 2016<sup>26</sup>.

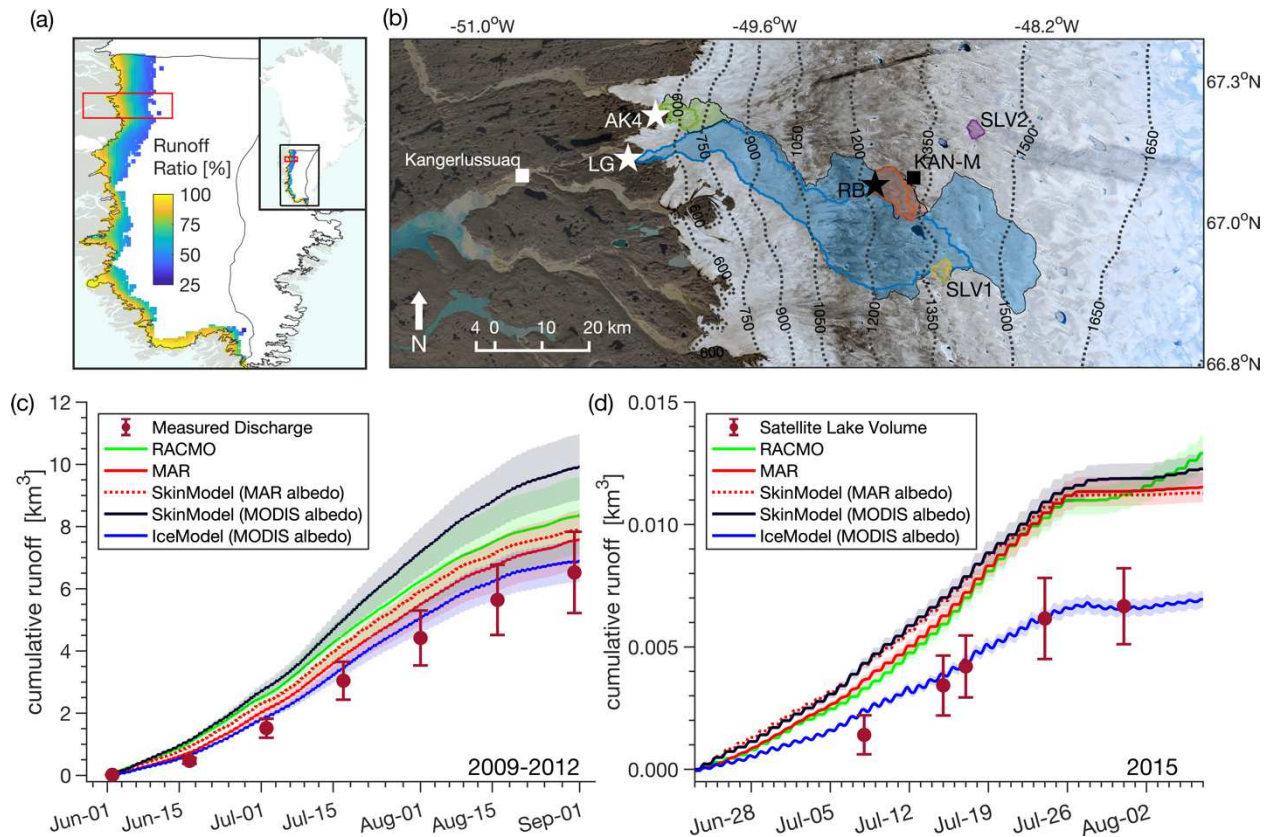


Figure 4: (a) IceModel simulations of meltwater runoff on the southwest Greenland Ice Sheet ablation zone from 2009–2018 suggest an annual average runoff reduction of  $\sim 11\text{--}23 \text{ Gt a}^{-1}$  due to meltwater refreezing in bare ice. Runoff ratios (ratio of runoff to meltwater production) vary from  $\sim 100\%$  near the ice sheet margin to  $\sim 25\%$  near the equilibrium line altitude. (b) Study area map showing upper and lower catchment boundaries and discharge gauge sites for the Rio Behar (RB) supraglacial catchment<sup>8</sup>, two supraglacial lake catchments with satellite lake volume (SLV1 and SLV2) runoff estimates<sup>12</sup>, the Leverett Glacier (LG) catchment<sup>42</sup>, and the Akuliarusiarsuup Kuaa River’s northern tributary (AK4) catchment<sup>48</sup>. Background image is Landsat 8 true-color composite on 26 July 2016. (c) Climate model runoff overpredicts four years of cumulative LG catchment discharge by +27% (RACMO2.3) and +15% (MAR3.10). Runoff predictions with our climate model emulator SkinModel forced with MODIS satellite ice albedo are +51% higher than observations, proxy for climate model predictions if forced with accurate ice albedo. IceModel simulations predict +5% higher runoff than observations. (d) Climate model runoff is +70% higher than satellite-derived runoff estimated from SLV infilling rate<sup>12</sup>, but are reconciled by IceModel simulations.

## Methods

### 1 Field datasets of ice sheet surface discharge, ablation rate, and ice density

Hourly Rio Behar catchment (Figure S1) discharges were measured during two field campaigns (20–23 July 2015 and 6–13 July 2016)<sup>8,34</sup> with a SonTek RiverSurveyor M9 Acoustic Doppler Current Profiler (ADCP) mounted on a SonTek HydroBoard II. The M9 was escorted across the Rio Behar main-stem channel with a bank-operated modified Tyrolean system with channel geometry and flow velocity measurements transmitted in real time to a bank-operated computer running the RiverSurveyor software. During each measurement hour, from 3–9 sub-hourly measurements and associated quality measures were recorded. These raw data were converted to channel flow rate [ $\text{m}^3 \text{s}^{-1}$ ] in post-processing following data quality-control workflows optimized for the supraglacial environment<sup>8,34</sup>. The sub-hourly measurements were used to estimate  $\sim \pm 15 \text{ m}^3 \text{ s}^{-1}$  measurement uncertainty (error bars in Figure 1 representing one standard deviation in sub-hourly discharge).

Measurements of ice surface elevation change were provided by a network of bamboo ablation stakes we installed at our field camp (67.049° N, 49.022° W), and by pressure transducer ice ablation assembly installed on the PROMICE/GAP KAN\_M automated weather station located  $\sim 2$  km from the Rio Behar catchment<sup>36</sup>. Twelve stakes were installed within an area covering  $\sim 0.5 \text{ km}^2$ . Stake locations were selected by generating random distance-direction pairs from a common center until a representative set of sites including bright white ice and dark impurity-laden ice were selected (Figure S2). Stakes were drilled 3 m deep into the ice and allowed to freeze-in for 24 hours prior to initiation of ablation stake measurements recorded at 3-hour intervals continuously from 12:00 on 6 July 2016 to 23:00 on 12 July 2016. Freeze-in was confirmed prior to each measurement to infer potential vertical displacement of these stakes due

to melt-out at their base (none occurred). Prior to each measurement, an 8-inch square wooden ablation board was placed at the base of the stake and oriented to true north. This board operated as a datum from which the stake height was measured. Cumulative changes in stake height were converted directly to ice surface elevation change for comparison with simulated melt rates. Field datasets of ice density from shallow ice cores, ice porosity, and ice liquid water saturation within excavated boreholes used to supplement this analysis are described in reference<sup>26</sup>.

## **2 Catchment boundaries and surface classification from satellite and airborne datasets**

Catchment topography and surface classification was provided by WorldView-1 and WorldView-2 satellite images of the ice sheet surface and aerial imagery collected with an RGB sensor mounted on an uncrewed aerial vehicle<sup>49</sup> (Figure S1). These aerial images were used to reconstruct the ice sheet surface topography using Agisoft PhotoScan Pro stereo-photogrammetry software and to perform surface classification of snow, water, and bare ice with a k-Nearest Neighbors algorithm yielding 2.7% snow cover during the 6–13 July 2016 field experiment, and 6.5% for the 20–23 July 2015 experiment<sup>8</sup> (Figure S1). WorldView-1 and WorldView-2 satellite imagery and associated high resolution stereo-photogrammetric digital elevation models were used to delineate the Rio Behar contributing catchment area following methods in reference<sup>8</sup>. Briefly, digital elevation based methods were supplemented with manual delineation of surface stream networks, flow direction, and channel heads following reference<sup>50</sup>. Interior channel heads (initiation points of channels that drain into the catchment) yield a minimum estimate of catchment area. Areas of internal drainage to moulins and crevasses that exist within the catchment boundary were removed from this lower catchment area estimate (Figure S1 and Figure S3). Outer channel heads (initiation points of channels that drain away from the catchment) yields an upper maximum estimate of catchment area. The optimal “best

guess” catchment area was delineated by tracing the inner and outer channel heads in the high-resolution WorldView imagery and adding back areas that undoubtedly flow into the catchment and subtracting areas that undoubtedly flow out of the catchment. This approach yields contributing catchment area confirmed by actively flowing water tracks, a further improvement to digital elevation model-based methods<sup>51</sup>. Identical methods were used to delineate the supraglacial lake contributing catchment areas for satellite lake volume (SLV1 and SLV2) retrievals, provided by reference<sup>12</sup>.

The Leverett Glacier (LG) catchment and Akuliarusiarsuup Kuua River’s northern tributary (AK4) catchment were defined using ice sheet catchment delineations provided with the PROMICE Greenland Liquid Water Discharge dataset<sup>44</sup>. These delineations used ArcticDEM v7 100 m gridded ice sheet surface topography and BedMachine v3<sup>52</sup> 150 m gridded ice thickness as input to the GRASS GIS software single-flow direction from eight neighbors (SFD-8) drainage basin delineation algorithm. For LG and AK4 catchments, upper, middle, and lower contributing area boundaries correspond to upper ( $k = 1.1$ ), middle ( $k = 1.0$ ), and lower ( $k = 0.9$ ) prescribed values of the flotation factor  $k$ , which accounts for evolving subglacial water pressure and hydraulic routing throughout the summer melt season<sup>44</sup>.

### **3 Climate model data**

Climate model output is from the polar version of the Regional Atmospheric Climate Model version 2.3 (RACMO2.3)<sup>22</sup>, the Modèle Atmosphérique Régional version 3.10 (MAR3.10)<sup>53</sup>, and the global climate model Modern-Era Retrospective analysis for Research and Applications, version 2 (MERRA-2)<sup>54</sup>. MAR3.10 data were provided at 15 km horizontal resolution and hourly timestep forced by European Centre for Medium-Range Weather Forecasts (ECMWF) ERA5 reanalysis<sup>55</sup>. RACMO2.3 data were provided at 11 km horizontal resolution

and 3-hourly timestep forced with ECMWF ERA-Interim reanalysis<sup>56</sup>. MERRA-2 data were provided on a global 0.5° by 0.625° latitude-longitude grid at 3-hourly timestep.

Hourly catchment runoff volumes for each model were extracted by intersecting the climate model horizontal grids with a bounding box that surrounds each catchment boundary  $\pm 0.06^\circ$  in latitude and  $\pm 0.04^\circ$  in longitude (Figure S3). These latitude and longitude coordinates were projected onto the National Snow and Ice Data Center Equal-Area Scalable Earth (EASE) version 2.0<sup>57</sup> coordinate system onto which the gridded climate model hourly runoff values were resampled at 100 m horizontal grid spacing using Delaunay triangulation and natural neighbor interpolation. The re-gridded values were then intersected with the catchment boundaries and converted to volumetric quantities using the catchment area-weighted average of the 100 m gridded values. This procedure was applied to all climate model output used in this study.

#### 4 SkinModel and IceModel description

SkinModel and IceModel solve the zero-dimensional surface energy balance<sup>58</sup>:

$$\chi Q_{si}(1 - \alpha) + Q_{li} - \varepsilon \sigma T_{sfc}^4 + Q_h + Q_e + Q_c = Q_m \quad (1)$$

where  $\chi$  [unitless] allocates the incoming shortwave solar radiation  $Q_{si}$  [ $\text{W m}^{-2}$ ] into a ‘skin’ surface component and a subsurface component,  $\alpha$  [unitless] is ice surface albedo,  $Q_{li}$  [ $\text{W m}^{-2}$ ] is incoming longwave radiation,  $\varepsilon \sigma T_{sfc}^4$  [ $\text{W m}^{-2}$ ] is longwave radiation emitted by the ice surface,  $\varepsilon=0.98$  [unitless] is ice surface emissivity,  $\sigma$  [ $\text{W m}^{-2} \text{K}^{-4}$ ] is the Stefan-Boltzmann constant,  $T_{sfc}$  [K] is ice surface temperature,  $Q_h$  [ $\text{W m}^{-2}$ ] is sensible heat flux,  $Q_e$  [ $\text{W m}^{-2}$ ] is latent heat flux,  $Q_c$  [ $\text{W m}^{-2}$ ] is conductive heat flux into the surface, and  $Q_m$  [ $\text{W m}^{-2}$ ] is energy available for meltwater production. For SkinModel simulations  $\chi = 1$  meaning all shortwave solar radiation is absorbed at the surface. For IceModel simulations  $\chi$  is the fraction of solar radiation absorbed at the top node of the one-dimensional ice column and is updated at each timestep with the

radiative transport model described below. Monin-Obukhov similarity theory is used to obtain  $Q_h$  and  $Q_e$  as described in reference<sup>35</sup>.

SkinModel calculates  $Q_c$  by solving the one-dimensional heat transfer equation with 2 cm node spacing to a depth of 20 m:

$$C_v \frac{\partial T_i}{\partial t} = -\frac{\partial Q_{c,i}}{\partial z} = \frac{\partial}{\partial z} \left[ k_i \frac{\partial T_i}{\partial z} \right] \quad (2)$$

where  $C_v$  [ $J m^{-3} K^{-1}$ ] is volumetric specific heat capacity,  $T_i$  [K] is ice temperature,  $k_i = 2.107 W m^{-1} K^{-1}$  is glacier ice thermal conductivity<sup>59</sup>, and  $z$  [m] is the vertical coordinate.

IceModel calculates  $Q_c$  and subsurface meltwater production/refreezing by solving the one-dimensional mass, thermal, and spectral radiative heat transfer equation<sup>35</sup>:

$$C_v \frac{\partial T_i}{\partial t} - \rho_i L_f \frac{\partial \theta_i}{\partial t} = \frac{\partial}{\partial z} \left[ (k_i + k_v) \frac{\partial T_i}{\partial z} \right] - \frac{\partial q}{\partial z} - C_v v_i \frac{\partial T_i}{\partial z} \quad (3)$$

where  $\rho_i$  [ $kg m^{-3}$ ] is ice density,  $L_f$  [ $J kg^{-1}$ ] is the latent heat of fusion of ice,  $\theta_i$  [ $m^3 m^{-3}$ ] is volumetric ice content,  $k_v$  is the water vapor diffusion coefficient for the ice matrix air passages, and  $v_i$  [ $m s^{-1}$ ] is the ice surface ablation rate. The model updates an earlier version<sup>35</sup> with field-calibrated values for the spectral absorption coefficient of ice<sup>60</sup> and a submodule for the  $v_i$  term following reference<sup>61</sup>. The upper boundary condition for Equation 2 and Equation 3 is  $T_{sfc}$ , which is estimated by solving Equation 1 by Newton-Raphson iteration<sup>35</sup>. The lower boundary condition is  $\partial T_i / \partial z = 0$ . Values for near-surface air temperature, wind speed, relative humidity, air pressure,  $\alpha$ , and  $Q_{si}$  and  $Q_{li}$  required to solve Equation 1 were provided by the KAN\_M automatic weather station on an hourly timestep for Rio Behar simulations and by MAR3.10 for regional simulations with daily  $\alpha$  from the PROMICE MODIS Greenland albedo product<sup>37</sup>.

The net solar flux  $\partial q / \partial z$  [ $W m^{-3}$ ] was evaluated with a two-stream radiative transfer model with 118 spectral bands<sup>35,62</sup>. A key input to this model is the solar radiation extinction

coefficient,  $\kappa$ , which controls the vertical distribution of absorbed solar radiation within ice. We constrained  $\kappa$  with our direct measurements of  $\partial q / \partial z$ <sup>32</sup>, which accounts for the melt-enhancing effect of dark impurities present within ice. The effect of ice impurities was further constrained by KAN\_M automatic weather station and MODIS albedo observations used as the upper boundary condition on the two-stream model (Supplementary Material).

## **5 Model simulations for Rio Behar and Southwest Greenland**

IceModel and SkinModel were solved on an hourly timestep at 100 m horizontal grid spacing for the experimental periods 6–13 July 2016 and 20–23 July 2015 for the ~60 km<sup>2</sup> Rio Behar catchment, with model input provided by the KAN\_M automatic weather station<sup>36</sup>. Regional-scale simulations for Greenland’s southwest sector (Figure 4) were solved on an hourly timestep at 5000 m horizontal grid spacing for the decade 2009–2018 with model input provided by MAR3.10 (the only model for which complete model forcing and evaluation data were provided). The model domain was Ice Sheet Mass Balance Intercomparison Experiment (IMBIE)<sup>1</sup> GrIS Southwest Sector, which covers ~12% of the ice sheet surface area but accounts for ~34% of modeled surface runoff<sup>15</sup>. IceModel and SkinModel values of bare ice runoff and refreezing were restricted to grid cells contained within the Greenland Ice Mapping Project (GIMP)<sup>63</sup> ice mask with Moderate Resolution Imaging Spectroradiometer (MODIS) daily ice surface albedo<sup>37</sup> <0.55 and >0.29 on at least 75% of days during July/August from 2000–2018 following references<sup>2,43</sup> to isolate bare-ice areas i.e., to remove firn/snow-covered grid cells and permanent land-surface. The 75% bare-ice frequency threshold is more restrictive than the 50% threshold used in the GrIS SMB Intercomparison (GrSMBMIP)<sup>43</sup>, and yields a conservative 37,175 km<sup>2</sup> bare-ice surface area for the Southwest sector, 22% lower than GrSMBMIP.

## **Data availability**

The data required to reproduce all figures in this manuscript are available without restriction from <https://github.com/mgcooper/icemodel>. Supraglacial river discharges for the Rio Behar catchment<sup>64</sup> are archived at the Arctic Data Center <https://doi.org/10.18739/A22F7JS1B>. MAR3.10 data are available on request from Dr. Xavier Fettweis. RACMO2.3.2 data are available on request from Dr. Willem Jan van de Berg. MERRA-2 data were provided by the NASA Goddard Earth Sciences and Data Information Services Center <https://disc.gsfc.nasa.gov/datasets?project=MERRA-2>. Automatic weather station data<sup>36</sup> and MODIS ice surface albedo<sup>37</sup> were provided by the Programme for Monitoring of the Greenland Ice Sheet <https://www.promice.org/PromiceDataPortal/>. Proglacial river discharges for Akuliarusiarsuup Kuua<sup>48</sup> are available from <https://doi.org/10.1594/PANGAEA.876357>. Proglacial river discharges for Leverett Glacier<sup>42</sup> are available from <https://doi.org/10.5285/17c400f1-ed6d-4d5a-a51f-aad9ee61ce3d>.

## **Code availability**

The numerical models and code required to reproduce all figures in this manuscript are available without restriction from <https://github.com/mgcooper/icemodel>.

## **Acknowledgements**

This project was funded by the NASA Cryospheric Science Program (grant 80NSSC19K0942) managed by Dr. Thorsten Markus, and a graduate fellowship from the NASA Earth and Space Sciences Fellowship Program (grant 80NSSC17K0374) managed by Dr. Lin Chambers. Charles Kershner (George Mason University), Sasha Z. Leidman (Rutgers University), and Rohi Muthyala (Rutgers University) contributed to field work. Polar Field Services and Kangerlussuaq International Science Support provided field logistical support.

## **Author Contributions**

M.G.C. wrote the manuscript and prepared the figures. M.G.C. and L.C.S. contributed equally to research design and manuscript editing. L.C.S., A.K.R., L.H.P., and B.T.O. designed the field experiment. L.C.S., A.K.R., L.H.P., B.T.O., M.G.C., J.C.R., C.M., S.W.C., and K.Y. carried out the field experiment. M.G.C. designed the model experiment with L.C.S. and G.E.L., wrote the numerical models with G.E.L., and performed the modeling. K.Y. performed the satellite lake volume runoff analysis. D.V.A. provided SEB model output. J.C.R. assisted with satellite classification of bare ice. All authors edited the manuscript and contributed to research questions.

## **Competing Interest Declaration**

The authors have no competing interests, financial or otherwise.

## References

1. Shepherd, A. *et al.* Mass balance of the Greenland Ice Sheet from 1992 to 2018. *Nature* **579**, 233–239 (2020).
2. Ryan, J. C. *et al.* Greenland Ice Sheet surface melt amplified by snowline migration and bare ice exposure. *Sci. Adv.* **5**, eaav3738 (2019).
3. Bevis, M. *et al.* Accelerating changes in ice mass within Greenland, and the ice sheet's sensitivity to atmospheric forcing. *PNAS* **116**, 1934–1939 (2019).
4. van den Broeke, M. R. *et al.* On the recent contribution of the Greenland ice sheet to sea level change. *The Cryosphere* **10**, 1933–1946 (2016).
5. Trusel, L. D. *et al.* Nonlinear rise in Greenland runoff in response to post-industrial Arctic warming. *Nature* **564**, 104–108 (2018).
6. Enderlin, E. M. *et al.* An improved mass budget for the Greenland ice sheet. *Geophys. Res. Lett.* **41**, 2013GL059010 (2014).
7. Rennermalm, A. K. *et al.* Evidence of meltwater retention within the Greenland ice sheet. *The Cryosphere* **7**, 1433–1445 (2013).
8. Smith, L. C. *et al.* Direct measurements of meltwater runoff on the Greenland ice sheet surface. *PNAS* **114**, E10622–E10631 (2017).
9. Overeem, I. *et al.* River inundation suggests ice-sheet runoff retention. *Journal of Glaciology* **61**, 776–788 (2015).
10. Mernild, S. H., Liston, G. E., van As, D., Hasholt, B. & Yde, J. C. High-resolution ice sheet surface mass-balance and spatiotemporal runoff simulations: Kangerlussuaq, west Greenland. *Arctic, Antarctic, and Alpine Research* **50**, S100008 (2018).

11. Smith, L. C. *et al.* Efficient meltwater drainage through supraglacial streams and rivers on the southwest Greenland ice sheet. *PNAS* **112**, 1001–1006 (2015).
12. Yang, K. *et al.* Surface meltwater runoff on the Greenland ice sheet estimated from remotely sensed supraglacial lake infilling rate. *Remote Sensing of Environment* **234**, 111459 (2019).
13. Lenaerts, J. T. M. *et al.* Representing Greenland ice sheet freshwater fluxes in climate models. *Geophys. Res. Lett.* **42**, 6373–6381 (2015).
14. Reijmer, C. H., van den Broeke, M. R., Fettweis, X., Ettema, J. & Stap, L. B. Refreezing on the Greenland ice sheet: a comparison of parameterizations. *The Cryosphere* **6**, 743–762 (2012).
15. Steger, C. R., Reijmer, C. H. & Broeke, M. R. van den. The modelled liquid water balance of the Greenland Ice Sheet. *The Cryosphere* **11**, 2507–2526 (2017).
16. MacFerrin, M. *et al.* Rapid expansion of Greenland’s low-permeability ice slabs. *Nature* **573**, 403–407 (2019).
17. Gardner, A. S. & Sharp, M. J. A review of snow and ice albedo and the development of a new physically based broadband albedo parameterization. *J. Geophys. Res.* **115**, F01009 (2010).
18. Noël, B., van de Berg, W. J., Lhermitte, S. & van den Broeke, M. R. Rapid ablation zone expansion amplifies north Greenland mass loss. *Sci. Adv.* **5**, eaaw0123 (2019).
19. Vizcaíno, M. *et al.* Coupled simulations of Greenland ice sheet and climate change up to AD 2300. *Geophys. Res. Lett.* **42**, 3927–3935 (2015).
20. Sutterley, T. C. *et al.* Evaluation of reconstructions of snow/ice melt in Greenland by regional atmospheric climate models using laser altimetry data. *Geophys. Res. Lett.* **45**, 8324–8333 (2018).

21. Noël, B. *et al.* Evaluation of the updated regional climate model RACMO2.3: summer snowfall impact on the Greenland Ice Sheet. *The Cryosphere* **9**, 1831–1844 (2015).
22. Noël, B. *et al.* Modelling the climate and surface mass balance of polar ice sheets using RACMO2 – Part 1: Greenland (1958–2016). *The Cryosphere* **12**, 811–831 (2018).
23. Sasgen, I. *et al.* Timing and origin of recent regional ice-mass loss in Greenland. *Earth and Planetary Science Letters* **333–334**, 293–303 (2012).
24. Xu, Z., Schrama, E. J. O., van der Wal, W., van den Broeke, M. & Enderlin, E. M. Improved GRACE regional mass balance estimates of the Greenland ice sheet cross-validated with the input–output method. *The Cryosphere* **10**, 895–912 (2016).
25. Koenig, L. S. *et al.* Wintertime storage of water in buried supraglacial lakes across the Greenland Ice Sheet. *The Cryosphere* **9**, 1333–1342 (2015).
26. Cooper, M. G. *et al.* Meltwater storage in low-density near-surface bare ice in the Greenland ice sheet ablation zone. *The Cryosphere* **12**, 955–970 (2018).
27. Kendrick, A. K. *et al.* Surface Meltwater Impounded by Seasonal Englacial Storage in West Greenland. *Geophys. Res. Lett.* **45**, 10,474–10,481 (2018).
28. Chu, W. *et al.* Extensive winter subglacial water storage beneath the Greenland Ice Sheet. *Geophys. Res. Lett.* **43**, 2016GL071538 (2016).
29. Lüthi, M. P. *et al.* Heat sources within the Greenland Ice Sheet: dissipation, temperate paleo-firn and cryo-hydrologic warming. *The Cryosphere* **9**, 245–253 (2015).
30. Harper, J., Humphrey, N., Pfeffer, W. T., Brown, J. & Fettweis, X. Greenland ice-sheet contribution to sea-level rise buffered by meltwater storage in firn. *Nature* **491**, 240–243 (2012).

31. Forster, R. R. *et al.* Extensive liquid meltwater storage in firn within the Greenland ice sheet. *Nature Geosci* **7**, 95–98 (2014).
32. Cooper, M. G. *et al.* Spectral attenuation coefficients from measurements of light transmission in bare ice on the Greenland Ice Sheet. *The Cryosphere* **15**, 1931–1953 (2021).
33. Yang, K. *et al.* A new surface meltwater routing model for use on the Greenland Ice Sheet surface. *The Cryosphere* **12**, 3791–3811 (2018).
34. Smith, L. C. *et al.* Supraglacial River Forcing of Subglacial Water Storage and Diurnal Ice Sheet Motion. *Geophys. Res. Lett.* **48**, e2020GL091418 (2021).
35. Liston, G. E., Winther, J.-G., Bruland, O., Elvehøy, H. & Sand, K. Below-surface ice melt on the coastal Antarctic ice sheet. *Journal of Glaciology* **45**, 273–285 (1999).
36. Fausto, R. S. & van As, D. Programme for monitoring of the Greenland ice sheet (PROMICE): Automatic weather station data. (2019) doi:10.22008/PROMICE/DATA/AWS.
37. Box, J. E., van As, D. & Steffen, K. Greenland, Canadian and Icelandic land-ice albedo grids (2000–2016). *GEUS Bulletin* **38**, 53–56 (2017).
38. Pitcher, L. H. & Smith, L. C. Supraglacial Streams and Rivers. *Annu. Rev. Earth Planet. Sci.* **47**, 421–452 (2019).
39. van den Broeke, M. R. *et al.* Partitioning of melt energy and meltwater fluxes in the ablation zone of the west Greenland ice sheet. *The Cryosphere* **2**, 179–189 (2008).
40. Stevens, I. T. *et al.* Near-surface hydraulic conductivity of northern hemisphere glaciers. *Hydrological Processes* **32**, 850–865 (2018).
41. Karlstrom, L., Zok, A. & Manga, M. Near-surface permeability in a supraglacial drainage basin on the Llewellyn Glacier, Juneau Icefield, British Columbia. *The Cryosphere* **8**, 537–546 (2014).

42. Tedstone, A. J. *et al.* Proglacial discharge measurements, Leverett Glacier, south-west Greenland (2009-2012). *Polar Data Centre, Natural Environment Research Council* (2017) doi:10.5285/17c400f1-ed6d-4d5a-a51f-aad9ee61ce3d.
43. Fettweis, X. *et al.* GrSMBMIP: intercomparison of the modelled 1980–2012 surface mass balance over the Greenland Ice Sheet. *The Cryosphere* **14**, 3935–3958 (2020).
44. Mankoff, K. D. *et al.* Greenland liquid water discharge from 1958 through 2019. *Earth System Science Data* **12**, 2811–2841 (2020).
45. Hastenrath, S. Diurnal thermal forcing and hydrological response of Lewis Glacier, Mount Kenya. *Arch. Met. Geoph. Biocl. A.* **32**, 361–373 (1983).
46. Ambach, W. Über den nächtlichen Wärmeumsatz der gefrorenen Gletscheroberfläche. *Arch. Met. Geoph. Biocl. A.* **8**, 411–426 (1955).
47. Holube, K. M., Zolles, T. & Born, A. Sources of Uncertainty in Greenland Surface Mass Balance in the 21<sup>st</sup> century. *The Cryosphere Discussions* 1–27 (2021) doi:10.5194/tc-2021-128.
48. Rennermalm, Å. K. *et al.* River discharge at station AK-004-001, 2008 - 2016, version 3.0. 1086494 data points (2017) doi:10.1594/PANGAEA.876357.
49. Ryan, J. C. *et al.* Dark zone of the Greenland Ice Sheet controlled by distributed biologically-active impurities. *Nature Communications* **9**, 1065 (2018).
50. Yang, K., Karlstrom, L., Smith, L. C. & Li, M. Automated High-Resolution Satellite Image Registration Using Supraglacial Rivers on the Greenland Ice Sheet. *IEEE Journal of Selected Topics in Applied Earth Observations and Remote Sensing* **10**, 845–856 (2017).
51. Yang, K., Smith, L. C., Chu, V. W., Gleason, C. J. & Li, M. A Caution on the Use of Surface Digital Elevation Models to Simulate Supraglacial Hydrology of the Greenland Ice Sheet.

- IEEE Journal of Selected Topics in Applied Earth Observations and Remote Sensing* **8**, 1–13 (2015).
52. Morlighem, M. *et al.* BedMachine v3: Complete Bed Topography and Ocean Bathymetry Mapping of Greenland From Multibeam Echo Sounding Combined With Mass Conservation. *Geophys. Res. Lett.* **44**, 11,051–11,061 (2017).
53. Fettweis, X. *et al.* Reconstructions of the 1900–2015 Greenland ice sheet surface mass balance using the regional climate MAR model. *The Cryosphere* **11**, 1015–1033 (2017).
54. Gelaro, R. *et al.* The Modern-Era Retrospective Analysis for Research and Applications, Version 2 (MERRA-2). *J. Climate* **30**, 5419–5454 (2017).
55. Delhasse, A. *et al.* Brief communication: Evaluation of the near-surface climate in ERA5 over the Greenland Ice Sheet. *The Cryosphere* **14**, 957–965 (2020).
56. Dee, D. P. *et al.* The ERA-Interim reanalysis: configuration and performance of the data assimilation system. *Q.J.R. Meteorol. Soc.* **137**, 553–597 (2011).
57. Brodzik, M. J., Billingsley, B., Haran, T., Raup, B. & Savoie, M. H. EASE-Grid 2.0: Incremental but Significant Improvements for Earth-Gridded Data Sets. *IJGI* **1**, 32–45 (2012).
58. Hoffman, M. J., Fountain, A. G. & Liston, G. E. Near-surface internal melting: a substantial mass loss on Antarctic Dry Valley glaciers. *Journal of Glaciology* **60**, 361–374 (2014).
59. Calonne, N. *et al.* Thermal Conductivity of Snow, Firm, and Porous Ice From 3-D Image-Based Computations. *Geophys. Res. Lett.* **46**, 13079–13089 (2019).
60. Warren, S. G. & Brandt, R. E. Optical constants of ice from the ultraviolet to the microwave: A revised compilation. *J. Geophys. Res.* **113**, D14220 (2008).

61. Jordan, R. *A One-Dimensional Temperature Model for a Snow Cover*. 49  
<https://hdl.handle.net/11681/11677> (1991).
62. Schlatter, T. W. The Local Surface Energy Balance and Subsurface Temperature Regime in Antarctica. *J. Appl. Meteor.* **11**, 1048–1062 (1972).
63. Howat, I. M., Negrete, A. & Smith, B. E. The Greenland Ice Mapping Project (GIMP) land classification and surface elevation data sets. *The Cryosphere* **8**, 1509–1518 (2014).
64. Smith, L. C. *et al.* Greenland Ice Sheet Acoustic Doppler Current Profiler (ADCP) measurements of supraglacial river discharge and Global Positioning System (GPS) measurements of ice surface motion. *Arctic Data Center* (2021) doi:10.18739/A22F7JS1B.

## Supplementary Files

This is a list of supplementary files associated with this preprint. Click to download.

- [cooperrefreezingsupp.docx](#)